Journal of Structural Geology, Vol. 14, No. 10, pp. 1121 to 1131, 1992
Printed in Great Britain

0191-8141/92 $05.00+0.00

Stress ratio determinations from striated faults: a spherical plot for cases of near-vertical principal stress

NORMAN FRY

Department of Geology, UWCC, P.O. Box 914, Cardiff CF1 3YE, U.K.

(*Received* 20 *May* 1991; *accepted in revised form* 7 *April* 1992)

Abstract—For stress regimes with one principal axis, z, vertical, the stress ratio is best represented by an angular function $F' = \arctan[\sqrt{3}(\sigma_z - (\sigma_{x_1} + \sigma_{x_2} + \sigma_z)/3)/(\sigma_{x_1} - \sigma_{x_2})]$, or if the larger of the horizontal principal stresses (σ_{x_1} and σ_{x_2}) is designated σ_y, by $F = \arctan[\sqrt{3}(\sigma_z - (\sigma_x + \sigma_y + \sigma_z)/3)/(\sigma_y - \sigma_x)]$. Traditional palaeostress regimes (normal, wrench, reverse) represent equal-angular sectors of F' or F, and may be subdivided. On a spherical projection of F against $2y$ (where y is the bearing of maximum horizontal stress), the locus of all combinations of stress orientation and stress ratio capable of generating one datum (known slip direction on a known fault plane) is a great circle, since $\tan F = -\cos(2y - (2s + b))/\sqrt{3}\cos b$, where $\tan b = \tan\omega/\cos d$, and s, d and ω are the fault strike, dip and striation pitch, respectively. Stereographic construction is simple using pencil and paper, and gives a visual appreciation of the definition of palaeostress states which could have generated the fault motions. It facilitates better than previous methods (1) the identification of radially symmetrical stress states; (2) recognition of suspect or incompatible data; and (3) delimiting the palaeostress state according to sense of shear, where this is known. Great circle and pole representations are suited to different purposes and data types, for which examples are given.

INTRODUCTION

SEVERAL authors have attempted to evaluate palaeostress regimes using populations of striated faults (e.g. Carey & Brunier 1974, Carey 1976, Armijo & Cisternas 1978, Angelier & Manoussis 1980, Etchecopar *et al.* 1981, Armijo *et al.* 1982, Angelier 1984, Carey-Gailhardis & Mercier 1987, Vergely *et al.* 1987, Célérier 1988, Will & Powell 1991). The two basic assumptions behind these methods are that striae on a fault record the direction of shear stress at the time of movement and that the stress regime is consistent (see Angelier 1989 and Mercier & Carey-Gailhardis 1989 for an appreciation of the latter point). Discrepancies are variously ascribed to errors of measurement or to fluctuations from these assumptions. Such methods often indicate that one principal stress is approximately vertical. By incorporating the Andersonian assumption of a vertical principal stress (here σ_z), the determination can be greatly simplified. There then exist only three degrees of freedom amongst the stress tensor (fully specified absolute magnitudes), the orientation of a fault plane and the shear direction of that plane. Simón-Gómez (1986), following Bott (1959) and Jaeger (1969), derives for each known fault orientation and striation pitch (rake) a residual univariant relationship, that of a ratio R of differences in principal stresses as a function of the bearing y of the σ_y axis ($\sigma_y > \sigma_x$). He then computes numerically the univariant (y, R) curve for each fault, converts each curve numerically to a new scale ($R^* = n(R/(R+1))$) and plots them together on a graph of R vs y (e.g. Fig. 1a). The point, or knot, of mutual intersections of any subset of the sampled faults specifies the y and R values of a mutually acceptable stress regime for that subset (Simón-Gómez 1986). Figure 1(a) shows the computed and rescaled (y, R) curves using

$$R = (\sigma_z - \sigma_x)/(\sigma_y - \sigma_x) = \sin^2\lambda - (\tan\theta \sin 2\lambda)/(2\cos\phi)$$

(Simón-Gómez 1986) for a hypothetical set of reverse faults (Table 1).

This paper proposes a new method based on a spherical representation. This combines graphical representation of the univariant relationship between orientation and stress ratio, following Simón-Gómez (1986), with use of an angular stress ratio function ($\arctan[\sqrt{3}(\sigma_z - (\sigma_x + \sigma_y + \sigma_z)/3)/(\sigma_y - \sigma_x)]$) following Armijo *et al.* (1982). The practical simplicity of this method is illustrated in Fig. 1. Curves describing the relationship between stress ratio and orientation for each fault become great circles, as in Fig. 1(b). It is only necessary to identify two points in order to specify and construct each curve. Furthermore, the same relationship may in this co-ordinate system be represented within one hemisphere by the poles to the circles of Fig. 1(b), as in Fig. 1(c). Each pole has the inclination c and azimuth ($2s + b + 180°$) given in Table 1. Their common great circle has itself a pole at inclination $= -60°$, $2y = 140°$, the point of intersection of the great circles in Fig. 1(b). The co-ordinates of this point represent the same mutually acceptable stress regime for the fault set as does the intersection at (070, −1) in the (y, R) diagram (Fig. 1a). Apart from calculating the values in

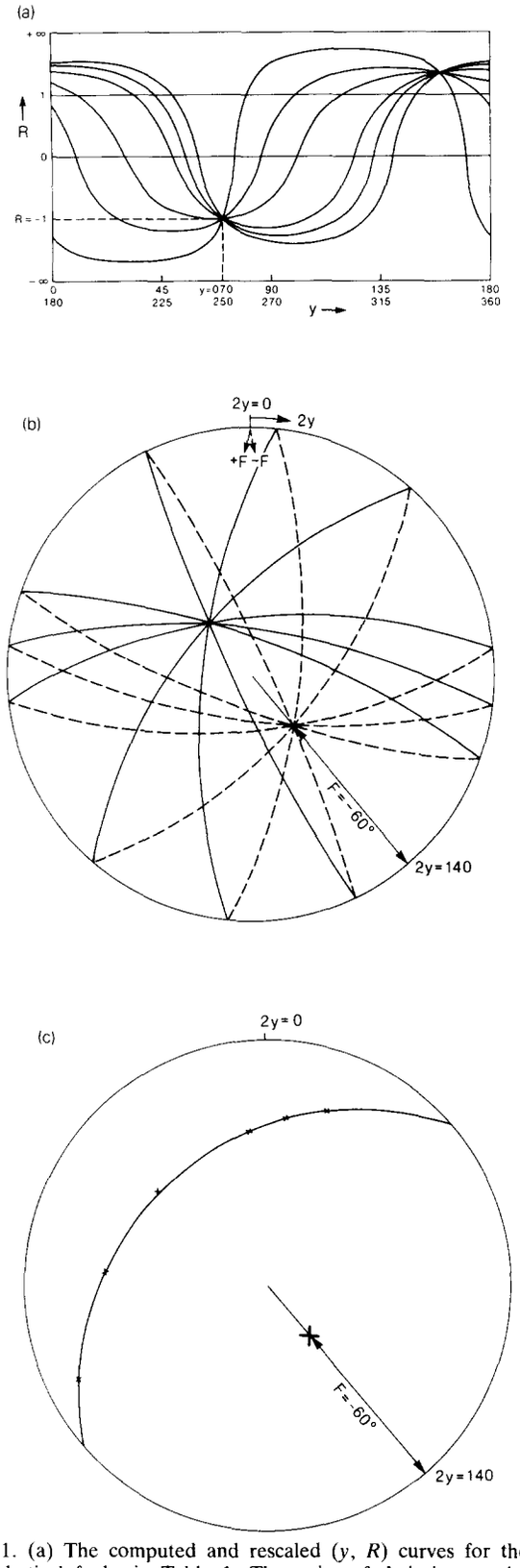

Fig. 1. (a) The computed and rescaled (y, R) curves for the six hypothetical faults in Table 1. The point of their intersection at $y = 070°$, $R = -1$ indicates that they could all have been generated by a reverse plane stress state with minimum horizontal stress equal to the mean of the vertical and maximum horizontal stresses, with the latter principal stress along 070–250°. (b) The same relationship as in (a) with each fault represented by a great circle on an (F, $2y$) stereogram, where inclination F represents stress ratio. Continuous lines are upper hemisphere, pecked lines lower hemisphere. The point of intersection at inclination $F = -60°$ and azimuth $2y = 140$ is the (F, $2y$) representation of the stress state described above. (c) The pole representation of the great circles in (b). Only the lower hemisphere is used if all faults have a reverse dip-slip component.

Table 1, no computation is necessary for either version of the proposed spherical representation. In contrast to (y, R) diagrams, it is not necessary to compute curves numerically, nor to rescale them, nor to use computer graphics.

THEORETICAL BASIS OF ANGULAR STRESS FUNCTIONS

Angular representation of stress ratio

The function of stress ratios appropriate to a given study of stress, and the best means of its graphical representation, will depend upon the assumptions behind the method. In this paper, the only assumption is that one principal stress direction is vertical. The *magnitudes* of the three principal stresses are of equivalent status, being equally unknown. The z principal stress is of unique status, because its *direction* is invariable, being defined as vertical; the other two directions of principal stresses are of equal status, being unrestricted within the horizontal plane. The *a priori* equivalence of the two horizontal principal stresses will be emphasized here by referring to them as σ_{x_1} and σ_{x_2}. An appropriate function of stress ratio will therefore be one which gives equivalent treatment to the three magnitudes of principal stresses, but which specifies the manner in which the one of unique direction departs from the other two.

Figure 2 shows the graphical representation of the relationship described above. Note that although the absolute magnitudes of stresses may be set by specifying a zero-stress base height and a scale, the relationship between angle of rotation and the ratios of stress differences is unaffected. This accords with the requirements addressed in this paper; methods employing the geometry of striation directions on faults do not constrain absolute magnitudes of stresses, only their ratio of differences. To illustrate this point further: we may consider the hypothesis of a constant mean stress by rotating the triangle in Fig. 2 about its centre. Alternatively, if we wish to assume constant vertical stress, due to gravitational load, we may rotate about the z apex. Each of these choices (or any other) leaves completely unaffected the relationship between *angle* of rotation and the *ratios* of stress differences of which the angle is a function.

Combined angular representation of stress ratio and orientation

The symmetry of the above treatment of principal stresses is significant.

(1) The three-fold rotational symmetry is the graphical representation of the equivalence of the three principal stresses in terms of magnitudes. Such symmetry and the equivalence it represents are not present in formulations such as $(\sigma_2 - \sigma_3)/(\sigma_1 - \sigma_3)$ (e.g. Angelier 1975,

Table 1. Data for a hypothetical set of six reverse faults, used to illustrate the comparison of the method proposed here with that of Simón-Gómez (1986) (Fig. 1). Striation pitch, or rake, ω, is measured clockwise from strike. The (y, R) curves in Fig. 1(a) are computed from the parameters shown. For the proposed method, no further computation is necessary

Fault No.	Data strike s	dip d	pitch ω	Method of Simón-Gómez $\phi = d$	$\theta = \lvert\omega\rvert$	$\frac{\tan\theta}{2\cos\phi}$	Method proposed $2s$	b*	$2s + b$	$-c$*
1	030	42	+64	42	64	1.38	060	71	131	29.4
2	086	56	−66	56	66	2.01	172	−76	096	22.7
3	124	60	−60	60	60	1.73	248	−74	174	25.5
4	170	84	+50	84	50	5.70	340	85	065	08.6
5	235	41	+73	41	73	2.17	110	77	187	21.3
6	320	76	−54	76	54	2.84	280	−80	200	16.7

*b = arctan (tan ω/cos d); c = arctan ($\sqrt{3}$ cos b).

1989) or $(\sigma_z - \sigma_x)/(\sigma_y - \sigma_x)$ (e.g. Armijo & Cisternas 1978, Simón-Gómez 1986).

(2) Rotation by 180° about the stress magnitude axis (up the plane of the paper of Fig. 2) swaps the two horizontal principal stresses, corresponding to a rotation of 90° about the vertical in real space.

(3) Action of a centre of symmetry reverses the sign of all stress differences. This represents changing the stress state to one which would precisely reverse striation directions on fault planes of all orientations.

To retain these properties, shown above to be appropriate to the assumptions behind the method, necessitates a three-dimensional graphical representation in which stress ratio is represented by an angle in the plane of Fig. 2 (analogous to latitude), and orientation of a horizontal reference direction of the stress tensor is represented by a double angle about the stress magnitude axis of Fig. 2 (analogous to longitude).

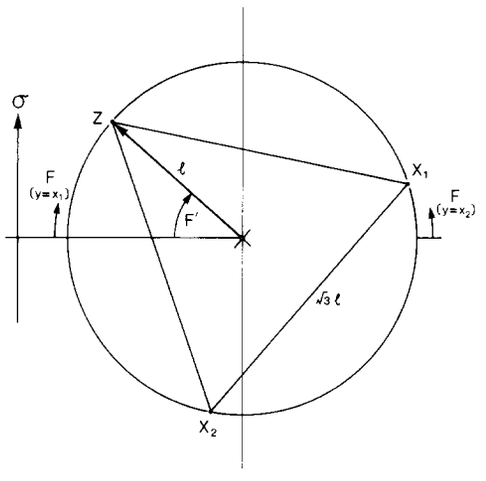

Fig. 2. Points representing the principal stress axes (here z, x_1 and x_2 in clockwise order) are marked equally spaced about a wheel. The magnitudes of their compressive stresses (σ) are on a vertical linear scale. Rotating the wheel provides an unbiased scan through all possible ratios of differences between σ values. Designating the radius as l the distance between apices is $\sqrt{3}l$. The case $\sigma_z = (\sigma_{x_1} + \sigma_{x_2} + \sigma_z)/3$ is chosen arbitrarily as the reference state, giving the angle F' as the unbiased measure of stress ratio throughout a complete rotation. With horizontal principal stresses σ_x and σ_y ($\sigma_y > \sigma_x$), the diagram splits into two sides. With z in the left half, $y = x_1$ and the modified angular function $F = F'$. With z in the right half, $y = x_2$ and F becomes $(180° - F')$. In both cases, F increases upwards on the diagram, with a range of −90° to +90°.

Choice of co-ordinates

The natural representations for such angular combinations described above is on the surface of a sphere. Its implementation requires a choice of spherical co-ordinates. The zero direction chosen here for the stress ratio function is the horizontal on Fig. 2, perpendicular to the stress magnitude axis. The angle labelled F' in Fig. 2 thus becomes the stress ratio function. Following previous workers, the chosen reference direction in the stress tensor is the direction of the maximum horizontal stress. The zero direction in the proposed spherical co-ordinate system is maximum horizontal stress towards north. Thus, the angle representative of stress tensor orientation on the spherical plot is $2y$, following the usage of y by Simón-Gómez (1986).

To specify the quantitative relationship between angle F' and the magnitudes of the principal stresses, we call the distance from the centre of the triangle to the z apex in Fig. 2 a length l. The distance separating apices representing σ_{x_1} and σ_{x_2} is $\sqrt{3}l$. After rotating an angle F' from the zero position:

$$\sigma_z - (\sigma_{x_1} + \sigma_{x_2} + \sigma_z)/3 = l \sin F'$$

$$\sigma_{x_1} - \sigma_{x_2} = \sqrt{3} l \cos F' \cdot$$

Therefore

$$\tan F' = \sqrt{3}\,(\sigma_z - (\sigma_{x_1} + \sigma_{x_2} + \sigma_z)/3) / (\sigma_{x_1} - \sigma_{x_2}), \quad (1)$$

where $-180° < F'(\pm N360°) < 180°$ and $\sigma_{x_2} > \sigma_{x_1}$. The choice of the maximum horizontal stress as the identified direction within the stress tensor introduces a distinction between the greater and lesser principal horizontal stresses and makes redundant angles of F' greater in absolute magnitude than 90°. This leads to a modified function F (Fig. 2), the same as θ of Armijo *et al.* (1982), where

$$\tan F = \sqrt{3}(\sigma_z - (\sigma_x + \sigma_y + \sigma_z)/3) / (\sigma_y - \sigma_x);$$

$$-90° \le F(\pm N360°) \le 90° \cdot \quad (2)$$

This is related to the R of Simón-Gómez (1986) by: $F = \arctan[(2R - 1)/\sqrt{3}]$.

Although readers may for practical purposes consider the angular function F to be merely a rescaling of their favourite stress ratio function, such as R of Simón-

Gómez (1986), its practical convenience arises from its theoretical appropriateness to the assumptions behind the method. It should be noted that the modification of F' to F does not destroy the symmetrical equivalence of the two horizontal principal stresses in the proposed spherical representation, merely of the co-ordinate frame imposed upon it.

Named stress regimes in terms of F *values*

Simón-Gómez (1986), following Bott (1959), divides the range in stress difference ratio R into three stress regimes. Harland & Bayly (1958) introduced further named regimes for conditions approximating to the uniaxial stress states (in the broad sense of being radially symmetrical about a single identifiable principal axis), at $R = -\infty$, $R = 0$, $R = 1$ and $R = +\infty$, which bound Bott's divisions. Armijo *et al.* (1982) point out that the angular function (F of this paper) displays Bott's stress regimes as precise 60° sectors (Fig. 3a). These bisect neatly into 30° subdivisions at plane stress states, providing the 13 named tectonic regimes in Fig. 3(b). Because these regimes are characterized by a function of stress ratio which encapsulates all potential combinations of fault orientation and slip vectors, it retains the symmetry of the stress tensor about its principal planes. Thus, for example, for every fault with sinistral motion there is a potential symmetrically identical fault of dextral motion. Therefore, the subdivision of the named regimes into 'sinistral' and 'dextral' subregimes (Bott 1959) on the basis of stress difference ratio is theoretically unsound. However, that is not to deny the possibility that one may discern empirically, for any dataset, that only an asymmetrical portion of the range of orientations permitted by stress ratios is actually represented.

MATHEMATICS OF THE SPHERICAL CO-ORDINATE SYSTEM

Symbols and conventions

It has already been assumed above that compressional stresses are positive, that the σ_z principal stress is vertical and that $\sigma_y > \sigma_x$. Values of angles are given in degrees where 360° is a complete rotation. The strike of a plane and the direction of the σ_y axis are given as positive clockwise bearings from north, denoted s and y, respectively. Readers may use their own conventions both for their range and for which end of these axes to record; the two-fold symmetry of the stress tensor about the assumed vertical principal axis ensures that the choice will make no difference to the determined stress regime. Dip, denoted d, is restricted to the range 0–90°.

Past workers have used the symbol R for several different stress ratios; it will only appear here in discussions of cited literature. The symbol 'ϕ', commonly used for angle of friction, has also been used for dip of a fault plane (e.g. Simón-Gómez 1986) and for stress ratio (e.g. Angelier 1975). The symbol 'θ' has been used for

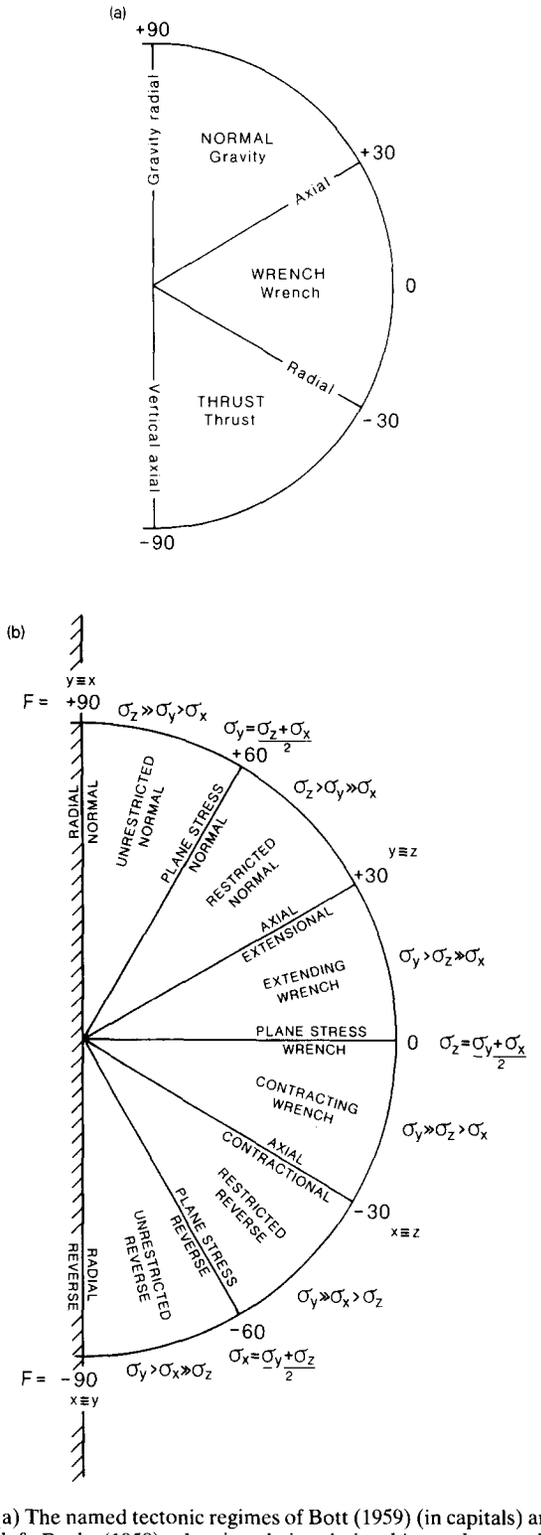

Fig. 3. (a) The named tectonic regimes of Bott (1959) (in capitals) and Harland & Bayly (1958), showing their relationship to the angular stress ratio function F. (b) Thirteen named tectonic regimes proposed here, with the broad three-fold division retained. Bott's term 'normal' is used, rather than 'gravity' of Harland & Bayly, for vertical compression exceeding compression in the horizontal plane. Their agreed term 'wrench' is retained for vertical compression within the range of that in the horizontal plane. 'Reverse' is introduced as being freer of unwarranted associations in its modern connotation than their term 'thrust' for vertical compression less than the horizontal compressional range. Subdivision of these broad 60° sectors of F is by addition of preceding terms, which may be omitted in cases where only the broad categorisation is appropriate. All names used are adjectival (e.g. 'extensional' rather than the noun form 'extension'), in recognition of the awkward fact that conditions of *stress* are here being distinguished on the basis of the *deformation* that they have the potential to induce.

striation pitch (Simón-Gómez 1986) and the stress ratio function favoured here (Armijo *et al.* 1982). These symbols will not be used in this paper.

Derivation of univariant equations in double angles

The three orthogonal co-ordinate frames in real space used in this derivation are shown in Fig. 4. Co-ordinates in the fault frame, particular to each individual fault, are related to the assumed common stress frame by

$$\begin{bmatrix} x'' \\ y'' \\ z'' \end{bmatrix} = \begin{bmatrix} \cos d & 0 & -\sin d \\ 0 & 1 & 0 \\ \sin d & 0 & \cos d \end{bmatrix} \times \begin{bmatrix} \cos\lambda & \sin\lambda & 0 \\ -\sin\lambda & \cos\lambda & 0 \\ 0 & 0 & 1 \end{bmatrix} \begin{bmatrix} x \\ y \\ z \end{bmatrix}. \quad (3)$$

The force on one side of a unit area of the fault plane is the vector sum of the components along the principal stress directions. Figure 5 illustrates the angular relationships between these directions and an element of the fault plane, which give the magnitudes of the components in the stress frame. Their vector sum can be represented by a line *to* the co-ordinate origin *from* a point having (x, y, z) co-ordinates $(\sin d \cos\lambda\ \sigma_x)$, $(\sin d \sin\lambda\ \sigma_y)$, $(\cos d\ \sigma_z)$. Substitution of these values in equation (3) gives the x'' and y'' components acting *from* down-dip and along strike, respectively.

$$x'' = \sin d \cos d \cos^2\lambda\ \sigma_x + \sin d \cos d \sin^2\lambda\ \sigma_y - \sin d \cos d\ \sigma_z$$

$$y'' = -\sin d \sin\lambda \cos\lambda\ \sigma_x + \sin d \sin\lambda \cos\lambda\ \sigma_y. \quad (4)$$

The angle of pitch of the shear stress on the fault plane has a tangent equal to the ratio of these two components.

Although the form of the above equations for shear stress components in the fault frame is the same as that of Jaeger (1969) and Simón-Gómez (1986), the sign conventions, ranges or definitions of most angles are different. The horizontal angle λ between fault and stress axes is defined here as $\lambda = y - s$ (Figs. 4 and 5). Its sign may be positive or negative, in agreement with Jaeger (1969), but contrary to the λ-positive convention of Simón-Gómez (1986). The ranges of y, s and λ are immaterial because all bearings are permitted both positive and negative values. The striation pitch on the fault plane will here be denoted ω, defined as the angle (clockwise-positive from above) from the y'' axis (strike). This is shown from positive-y'' in Fig. 5, whereas Jaeger (1969) defines ω clockwise-positive from the negative-y'' axis; the difference is of no consequence because the same value of $\tan\omega$ results. Jaeger's symbol ω is chosen intentionally, to distinguish it from θ, which Simón-Gómez (1986) defines as positive in reverse faults and negative in normal faults. Both the sense of shear and the range of ω are immaterial to the following derivation.

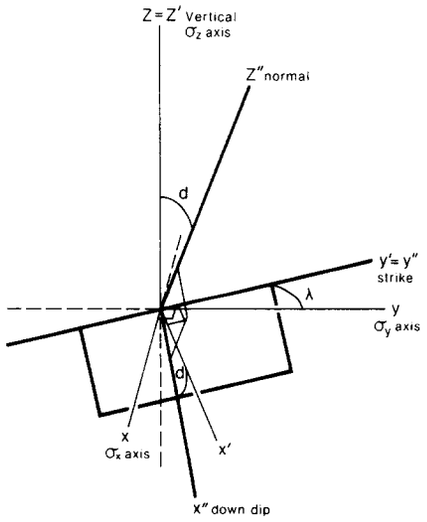

Fig. 4. The three sets of orthogonal co-ordinate axes used to obtain equation (3). Those denoted (x'', y'', z'') are different for each fault and must be related to the assumed common stress axes (x, y, z). The dip d is measured for each fault, but the horizontal angle λ is the difference between the maximum horizontal stress direction (to be determined) and the measured strike of the individual fault.

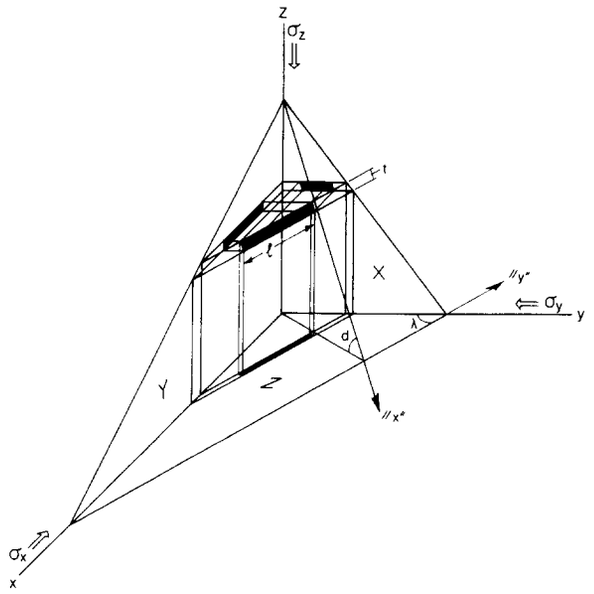

Fig. 5. Angles to principal stresses of an element of the fault plane having horizontal length l and thickness t. Its projected dimensions are: $t \sin d\ l \cos\lambda$ on plane X; $t \sin d\ l \sin\lambda$ on plane Y; $t \cos d\ l$ on plane Z. The component of force acting on the element along each principal stress direction is the product of principal stress magnitude and projected area presented perpendicular to that axis. Dividing by tl gives the components *per unit area* of the plane as $(\sin d \cos\lambda\ \sigma_x)$ along x, $(\sin d \sin\lambda\ \sigma_y)$ along y, and $(\cos d\ \sigma_z)$ along z.

Relating ω to components of shear stress:

$$\tan\omega = \frac{x''}{y''} = \frac{2x''}{2y''} = \frac{\sin d}{\sin d} \times \frac{\cos d \cdot 2(-\sigma_z + \cos^2\lambda\ \sigma_x + \sin^2\lambda\ \sigma_y)}{2 \sin\lambda \cos\lambda(\sigma_y - \sigma_x)}$$

$$= \frac{\cos d}{2 \sin\lambda \cos\lambda} \times \left[\frac{-(2\sigma_z - 2\cos^2\lambda\ \sigma_x - 2\sin^2\lambda\ \sigma_y)}{(\sigma_y - \sigma_x)}\right]$$

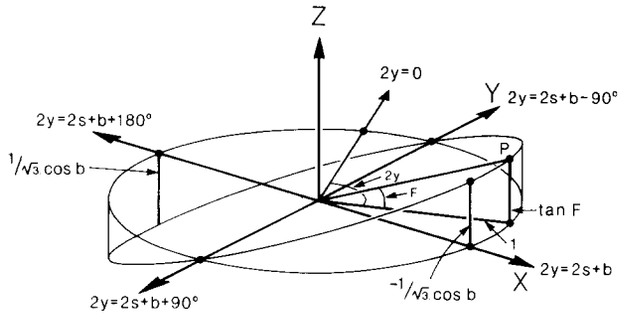

Fig. 6. The locus of points (P) obeying the relationship of equation (5), lie on a tilted section of a vertical cylinder, where the value ($2y$) is represented as the angle of a unit radius from $2y = 0$ in the horizontal plane and tan$F$ is a linear vertical scale. The proportionality of 'local' X and Z co-ordinates of P is used in the text to demonstrate that the locus for equation (5) is contained in a plane of tilt arctan($1/\sqrt{3}\cos b$) about a horizontal diameter at $2y = (2s + b) \pm 90°$.

$$= \frac{-\cos d}{\sin 2\lambda}$$

$$\times \frac{(3\sigma_z - \sigma_z) - ([2\cos^2\lambda - 1]\sigma_x + \sigma_x) + ([1 - 2\sin^2\lambda]\sigma_y - \sigma_y)}{(\sigma_y - \sigma_x)}.$$

Replacing $[2\cos^2\lambda - 1]$ and $[1 - 2\sin^2\lambda]$ by $\cos 2\lambda$ gives

$$\frac{-\sin 2\lambda \tan\omega}{\cos d} = \left[\frac{3\sigma_z - (\sigma_x + \sigma_y + \sigma_z)}{(\sigma_y - \sigma_x)} + \frac{\cos 2\lambda\,(\sigma_y - \sigma_x)}{(\sigma_y - \sigma_x)}\right].$$

Using equation (2), this gives

$$\frac{-\sin 2\lambda \tan\omega}{\cos d} = \sqrt{3}\tan F + \cos 2\lambda \cdot$$

Defining $\tan b = \tan\omega/\cos d$ and rearranging gives

$$-\sqrt{3}\tan F = \cos 2\lambda + \sin 2\lambda \tan b$$
$$= (\cos 2\lambda \cos b + \sin 2\lambda \sin b)/\cos b$$
$$= \cos(2\lambda - b)/\cos b.$$

Rearranging with 2λ replaced by $(2y - 2s)$ gives

$$\tan F = -\frac{1}{\sqrt{3}} \frac{\cos(2y - (2s + b))}{\cos b}. \qquad (5)$$

As s and b are known from measurement, this represents a cosine curve for the univariant relationship between tan F, specifying stress ratio and $2y$, double the bearing of the greater horizontal principal compression (σ_y).

Locus of univariant equations in spherical representation

In the three-dimensional geometry introduced earlier, any $2y$ is represented by a horizontal line at angle $2y$ from a $2y = 0$ (i.e. σ_y N–S) reference direction. If a line of unit length is used, the locus of all σ_y directions is a horizontal circle of unit radius (Fig. 6). For each fault, there is a horizontal diameter at $2y = (2s + b) \pm 90°$ for which $\tan F = 0$, and one perpendicular at $2y = (2s + b)$; $2y = (2s + b) + 180°$ for which tan$F$ has its maximum and minimum values, respectively (equation 5). For the remainder of this paragraph, these horizontal diameters are taken as local (X, Y, Z) co-ordinate axes, with positive X along $2y = (2s + b)$, positive Y along $2y = (2s + b) - 90°$ and positive Z vertical, 'local' in the sense of particular to one represented fault. Any radius representing a $2y$ value lies at angle $2y - (2s + b)$ from the local X axis, and its extremity has local (X, Y) co-ordinates of $(\cos(2y - (2s + b)), -\sin(2y - (2s + b)))$. We can now represent the value of tan$F$ by a vertical height (equation 5) of

$$Z = \tan F = (-1/(\sqrt{3}\cos b))\cos(2y - (2s + b)) \cdot$$

Note first that the local X and Z co-ordinates are proportional, such that any point (X, Y, Z) representing a fault must lie on a plane of tilt arctan $(1/(\sqrt{3}\cos b))$ which contains the horizontal Y axis (Fig. 6), and secondly that the direction from the origin to each (X, Y, Z) point can be specified relative to universal co-ordinates by its inclination F and azimuth $2y$. Superimposing a sphere of unit radius, the locus on the (F, $2y$) sphere of all possible (F, $2y$) values for one fault datum becomes the intersection of the sphere with the plane of tilt arctan$(1/(\sqrt{3}\cos b)$ about horizontal diameter $2y = (2s + b) \pm 90°$. Thus, *each fault datum is represented by a great circle.*

PROPERTIES OF THE SPHERICAL REPRESENTATION

The spherical representation described in this paper has some advantages in interpretation over the (y, R) curves of Simón-Gómez (1986). These mostly relate to three particular issues dealt with separately below. The first two issues concern the appropriateness of the spherical topology. Consider the three-dimensional stress state. As the values of the two horizontal principal stresses converge, more happens than simply σ_x and σ_y becoming the same value. Their identities are defined by ($\sigma_y > \sigma_x$). Given any interval of error in their magnitudes, our confidence in the correct identification of σ_x and σ_y decreases as their values converge. Furthermore, the identity of these discrete principal axes requires anisotropy of stress in the horizontal plane. As σ_x and σ_y converge to a common value, we progressively lose confidence in their directions until, in the limit, rather than saying $\sigma_y = \sigma_x$, we should recognize that all horizontal directions are equal in status. These characteristics of the stress state are represented topologically on an (F, $2y$) sphere. As σ_x and σ_y converge at $F = \pm 90°$, the representation attains radial symmetry in the horizontal plane.

Representation about horizontal isotropy

The advantages of the spherical plot around $\sigma_y = \sigma_x$ are listed here and illustrated in Fig. 7.

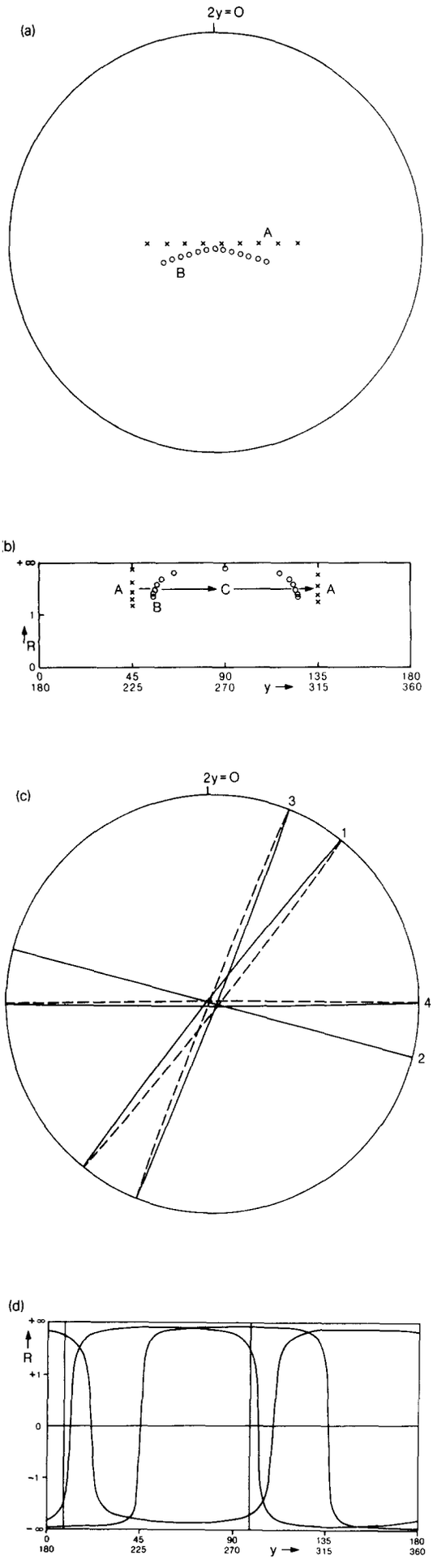

Fig. 7. A comparison of the (y, R) and $(F, 2y)$ representations of stress conditions approaching those of radial symmetry about the vertical stress axis. (a) Stereogram of $(F, 2y)$ for two sets of values, each having a series of small stepwise changes in stress conditions. Set A is characterized by constant *orientation* of all the stress axes, although the *magnitudes* of the horizontal principal stresses cross. The latter causes a switch between the designations as σ_x and σ_y axes ($\sigma_y > \sigma_x$), accompanied by a jump in $2y$ from 090° to 270°, but the constant axial bearings and the gradual nature of the changes are faithfully represented. Note the correctness of the indeterminacy of the value $(2y)$ at $F = 90°$, because the topology of the $(F, 2y)$ sphere around this condition accords with that of the stress state. Set B has gradual change of both orientations and magnitudes. (b) The upper $(R > 0)$ half of the (y, R) diagram for the same sets as (a). Note how the two fractions of set A appear to be unrelated; such a representation invites the postulation of a (y, R) path, such as C, through intermediate y values between these fractions, whereas no real rotation of principal stresses has occurred. Note the stretching out of set B as it approaches infinite R. (c) The $(F, 2y)$ stereogram (both hemispheres), using great circle representation, for faults 1–4 of Table 2. Their 'knot' at conditions indicative of a 'radial' stress regime with constant stress in the horizontal plane ('radial normal' or 'radial reverse') is clearly identifiable. Such a knot at $F \approx \pm 90°$ could either indicate a genuine palaeostress regime, as in Fig. 10, or alert us, as in this case, to data with $d \approx 90°$; $\omega \neq 0$. Such data contradict the assumption of vertical principal stress. (d) The (y, R) diagram for the same faults to show how the intersections of the equivalent lines to those in (c) are spaced out horizontally, making the identification of knots near to $R = \pm\infty$ dependent on the user's appreciation of the distortion of the plot (whether or not such fault sets indicate a genuine palaeostress regime).

(1) No numerical rescaling is needed to keep the plot in finite bounds as $\sigma_x \rightarrow \sigma_y$ (i.e. $F \rightarrow 90°$ whereas $R \rightarrow \infty$).

(2) The indeterminacy of bearing y as $\sigma_x \rightarrow \sigma_y$ is an integral feature of the plot, not dependent on the particular curves of faults sampled.

(3) Knots around $F = \pm 90°$ are easily visible because distances between intersections have not suffered horizontal magnification.

(4) Swapping of σ_x and σ_y is truthfully displayed as a gradational change in values.

(5) Spurious intermediate stress orientations are avoided.

Ghost knots

The purpose of constructing the univariant curves for fault data is to find the co-ordinates of their intersection—the value of stress ratio and orientation capable of generating all the striated faults with curves contributing to that intersection. More typically, the intersection of the curves will not be exact; instead the curves will all pass close to a representative value of stress ratio and orientation, giving a cluster of mutual intersections ('knot') in its vicinity. Individual deviations from the representative value may arise from errors of measurement, or from real variations in stress ratio and orientation. An advantage of graphical methods is that it is not necessary to make assumptions about deviations. Provided they are small, i.e. the knot is tight, the representative value is considered a sufficient approximation to the stress regime. However, there are three other circumstances which give rise to 'knots' irrespective of stress regime. The spherical representation facilitates their identification and consequently the avoidance of erroneous interpretation. One

circumstance arises from errors; the other two are an integral feature of any striation pitch method which subsumes the magnitude and sign of shear stress components within their ratio, as a means of handling the angle of pitch of the striations. A procedure which eliminates these latter two types will be outlined later.

(1) *Knots at* F = ±90° (R = ±∞ *on a* (y, R) *plot*). A remarkable feature of these methods is their insensitivity to errors. For faults dipping <45°, up to 20° departure from the assumed verticality of one principal axis leads to <10° error in (F, $2y$). A full treatment of errors is complicated and does little more than justify a pragmatic approach which may be summarized as follows.

(i) For a particular fault, errors of measurement of angles d and ω result in angular errors of similar or lower magnitude (×2 or less) in F and $2y$, unless $|\omega| < 30°$ and $d > 80°$;

(ii) For a set of faults, any outcome due to gross errors is likely to be failure to determine a knot indicative of their common stress regime.

The one important exception to these generalizations arises with data which contradict the symmetry assumptions of the method. Because z is assumed vertical, all vertical faults ($d \approx 90°$) should display a horizontal mirror plane of symmetry; only horizontal striations ($\omega \approx 0$) are permitted. All obliquely striated vertical fault planes ($d \approx 90°$; $\omega \neq 0$) included in a data set will combine in a knot at $F \approx \pm 90°$, as in Fig. 7(c).

The counterintuitive effect of the calculations with regard to vertical faults is worthy of comment. If the data *are not* consistent with the assumptions of the method in that ω values are non-zero, a real value of ±90° is determined for b, hence also for F for all ($2y$) except at $2y = (2s + b) \pm 90°$, when F is indeterminate and can take any value. This corresponds graphically to stating that a vertical (F, $2y$) great circle *can* be drawn at $2y = (2s + b) \pm 90°$. On the other hand, if the data *are* consistent ($\omega = 0$), b and hence F are indeterminate for all ($2y$), and *no circle can be drawn*. In fact, any stress regime plotting anywhere on the sphere (apart from a vanishingly small area along $2y = 2s$; $2y = 2s \pm 180°$) is capable of generating horizontal shear stress on a vertical fault, and so none can be favoured and represented as a great circle.

In practice, vertical faults should be considered important, not because they will help to constrain F or $2y$, but because the closeness to horizontal of their striations indicates the accuracy of the assumption that a principal stress axis was vertical.

(2) *Knots at* F = ±30° (R = 0, R = 1 *on a* (y, R) *plot*). Every great circle of

$$\tan F = (-1/(\sqrt{3}\cos b))\cos(2y - (2s + b))$$

passes through $F = -30°$ for σ_y along strike ($2y = 2s$) and $F = +30°$ for σ_x along strike ($2y = 2s \pm 180°$). Therefore, if several faults share the same strike (including those of opposed dip) their (F, $2y$) great circles must all pass through the same points at ($-30°$, $2s$) and ($+30°$, $2s + 180°$). If these faults *do* belong to the same stress regime, the circles should run together right around the sphere and *no* particular concentrations of intersections will be identifiable as indicating their generating (F, $2y$) value. If their fault motions are *not consistent* with a common generating stress regime, they will spread out from *clearly definable knots at* ±30°, as in Fig. 8. Therefore, knots at ±30°, at $2y = 2s$ cannot be taken to indicate any value of F; they indicate a common strike direction *and a lack of common stress regime*. Faults sharing strike direction are common in crystalline basement and its overlying cover in many regions, so ghost knots of this type are likely to be encountered.

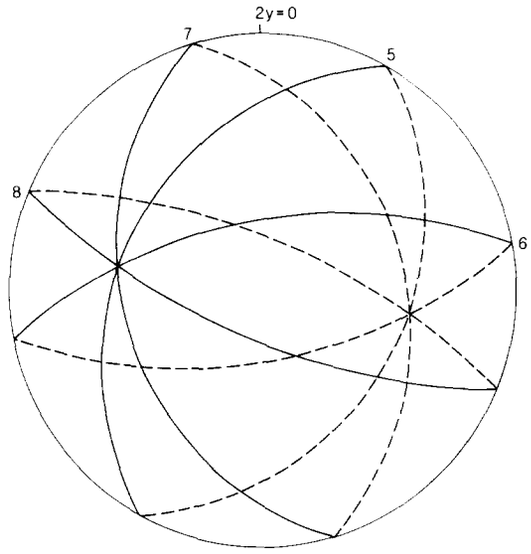

Fig. 8. The (F, $2y$) stereogram (both hemispheres), using great circle representation, for faults 5–8 of Table 2. The circles 'knot' at (−30°, 100°) and (+30°, 280°), indicative of mutually acceptable 'axial' stress regimes. Such knots at $F = \pm 30°$ could either indicate a genuine palaeostress regime or, as in this case, alert us to a set of faults with *common strike and different generating stress states*.

Table 2. Data for Figs. 7(c) & (d) and 8 to illustrate 'ghost knots'

Fig. No.	Fault No.	strike s	dip d	pitch ω
7(c) & (d)	1	021	88	45
	2	053	90	45
	3	102	89	45
	4	136	89	45
8	5	050	10	20
	6	050	10	70
	7	050	40	−20
	8	050	58	−66

(3) *Complementary knots at opposite points on the sphere*. If a group of great circles intersect at a knot on a

sphere, they also intersect at the opposite point. (This is true whether the intersection is genuine, as Fig. 1b, or not, as Figs. 7c and 8.) All the shear directions on all faults generated by one of the indicated stress regimes would be precisely reversed for the other. Therefore, we can only expect to constrain $(F, 2y)$ (or its y, R equivalent) to a complementary pair of possible values by the methods described up to this point in the paper. To identify which pair of points is appropriate, it is necessary to descriminate on the basis of recorded shear senses. For the example in Fig. 1, all faults had a reverse component, and it was therefore trivial to plot and determine the pole in the lower (horizontally contractional) hemisphere, entirely without using the upper (horizontally extensional) hemisphere. For fault sets closer to a wrench regime, it is preferable to modify the method to take detailed account of shear senses, as described in the following section.

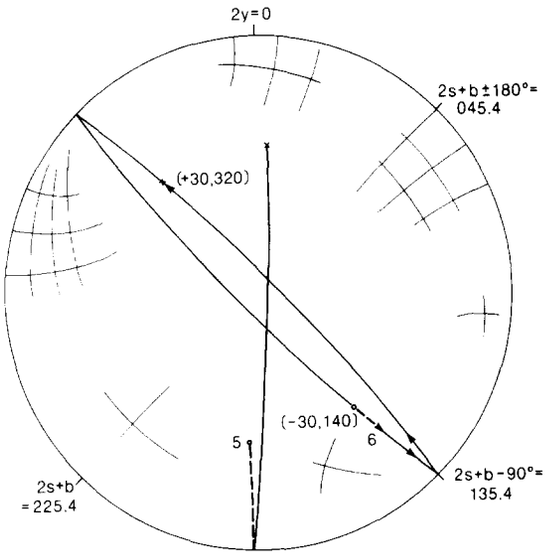

Fig. 9. The procedure for plotting half great circles of the correct shear sense. The half great circle for fault 5 of Table 3 has already been drawn. That for fault 6 of Table 3 has the locations of $(-30°, 2s)$ and $(+30°, 2s + 180°)$ marked, and is now aligned with a stereographic net, ready to trace in its half great circle. This will be drawn *anticlockwise* through $(0, 2s + b - 90°)$ because the horizontal component of shear is *sinistral*.

INCORPORATING DISCRIMINATION OF SHEAR SENSE INTO THE METHOD

The choice between two complementary values of stress ratio requires knowledge and use of the sense of shear on the striated faults. Previous workers have suggested different approaches.

Simón-Gómez (1986) makes use of procedures which are external to his (y, R) method to "delimit an interval in which the σ_y axis . . . is compatible with all fault movements". This may be appropriate with simple datasets, because some of the methods available to test the validity of the assumption of a vertical principal stress provide the required information (e.g. Angelier & Mechler 1977, Lisle 1987, 1988). It may not be satisfactory if the data include faults produced in several different stress regimes.

Maxwell (1990) describes each fault as 'sinistral', 'dextral', 'normal' or 'reverse' and restricts each (y, R) curve to a sector compatible with this characterization.

In this paper, it is suggested that the $(F, 2y)$ great circle representing each fault should be restricted to *that half which is consistent with the recorded shear sense for that particular fault*, where the latter has been determined. This is most easily explained by considering the strike component of shear on a dipping fault plane. This will be dextral (positive y'' in equation 4) for $0° < \lambda(\pm N180°) < 90°$ and sinistral for $90° < \lambda(\pm N180°) < 180°$. Shear stress passes through zero magnitude at $\lambda = N90°$, at which the stress state on the fault plane has bilateral symmetry about a vertical plane, thus ruling out non-zero shear stress (unless measured $\omega = 90°$).

Translated to the $(F, 2y)$ sphere, this means that each great circle is divided into a dextral half $(2s < 2y < 2s + 180°)$, and a sinistral half $(2s + 180° < 2y < 2s + 360°)$, separated by zero shear stress points at $(-30°, 2s)$ and $(+30°, 2s + 180°)$. Thus, it is easy to adopt a plotting procedure on a stereogram of both hemispheres which incorporates shear sense for every fault. *This is the advised procedure for general use of the* (F, 2y) *spherical plot and is as follows* (illustrated by Fig. 9):

Table 3. Data from near Zaragoza, Spain, kindly supplied by R. J. Lisle, used for Figs. 9 and 10 to illustrate the discussion on the use of $(F, 2y)$ plots. The shear sense of every fault includes a normal dip-slip component; hence positive ω indicates a sinistral horizontal component and negative ω indicates a dextral component

Fault No.	s	d	ω	$2s$	b	$2s+b$
1	119	88	90	238	90.0	328.0
2	125	59	90	250	90.0	340.0
3	151	65	+88	302	89.2	031.2
4	135	50	90	270	90.0	360.0
5	92	84	+70	184	87.8	271.8
6	70	79	+67	140	85.4	225.4
7	150	62	−84	300	−87.2	212.8
8	136	80	+85	272	89.1	001.1
9	59	66	+88	118	89.2	207.2
10	292	87	−84	224	−89.7	134.3
11	218	70	+82	076	87.3	163.3

(1) calculate $2s$, $b = \arctan(\tan\omega/\cos d)$ and $(2s + b)$, as in Table 3;

(2) locate points $(-30°, 2s)$ and $(0, 2s + b + 90°)$ and their opposites at $(+30°, 2s + 180°)$ and $(0, 2s + b - 90°)$;

(3) draw half a great circle *from* $(-30°, 2s)$ *either clockwise if dextral or anticlockwise if sinistral*, along the great circle which passes *through* $(0, 2s + b \pm 90°)$ *as far as* $(+30°, 2s + 180°)$.

In interpreting the resulting stereogram, any semi-circle which ends within a knot should not be considered to contribute to it (see below).

Using this procedure, semi-circles will only knot at the $(F, 2y)$ regime of appropriate shear sense for *every* fault, thus avoiding the complementary 'ghost knots' previously described. A semi-circle ending at a knot indicates that the stress regime of the knot would provide a

shear stress close to zero magnitude, not appropriate for the fault motion, with a principal stress axis lying very close to strike ($2y = 2s$). Thus, discounting the ends of the semi-circles will avoid the strike-parallel 'ghost knots' at $F = \pm 30°$ previously considered.

A special procedure which may be adopted in the case that every fault in the data set has the same sense of dip-slip component (either all normal or all reverse) is to calculate and plot the poles to the $(F, 2y)$ great circles and then to choose a great circle to fit these plotted points, as in the example in Fig. 1(c). For normal faults, only the upper hemisphere is needed, each pole having azimuth of $(2s + b)$ and inclination $c = \arctan(\sqrt{3}\cos b)$. For reverse faults, only the lower hemisphere is needed and the azimuth is $(2s + b + 180°)$. The pole to the fitted great circle *which lies in the plotted hemisphere* has the $(F, 2y)$ co-ordinates of the palaeostress regime suitable for generating all the faults which fit the circle.

EXAMPLE AND DISCUSSION

Table 3 is a subset of some fault data provided courtesy of R. J. Lisle which has been plotted using both half great circle and pole procedures (Fig. 10). The knot of Fig. 10(a) is clearly well defined and close to $F = +90°$. The poles on Fig. 10(b) clearly lie so close to the horizontal ($F = 0$) plane that the pole to their great circle would correspond in position to the knot in Fig. 10(a), as it should.

Each plotting procedure has some advantages as regards visual appreciation. The semi-circle diagram gets cluttered with lines with only a small number of faults (11 in Fig. 10a), making the pole diagram a more acceptable way to *display* such information. On the other hand, the exact spread of all possible intersections, and the drop off in intersection density away from the centre of the knot is only seen with the semi-circle diagram. The semi-circle diagram gives a better visual impression of the closeness of correspondence of nearly vertical $(F, 2y)$ loci where these are of opposed tilt, such as faults 3 and 7 with their poles in NE and SW quadrants, respectively, but only 2° difference in $2s$. It also displays the limited range of overlap permitted for some pairs of loci, such as 7 and 9, which have close $(F, 2y)$ poles (close $(2s + b)$), but almost perpendicular strikes, s. The conclusion to be drawn is that *the semi-circle diagram is generally a better working tool* than the pole diagram for any but the simplest data set, such as perhaps that used for Fig. 10.

A couple of observations can be made about the interpretation of semi-circle $(F, 2y)$ diagrams. These arise from the obvious point that however many intersections a semi-circle may have with others on the diagram, the fault it represents only had one generating palaeostress condition.

(1) If the same bundle of curves makes a substantial contribution to more than one knot, all but one of the knots is probably incidental (as would appear to be the proper interpretation of figs. 2b and 5b of Simón-Gómez

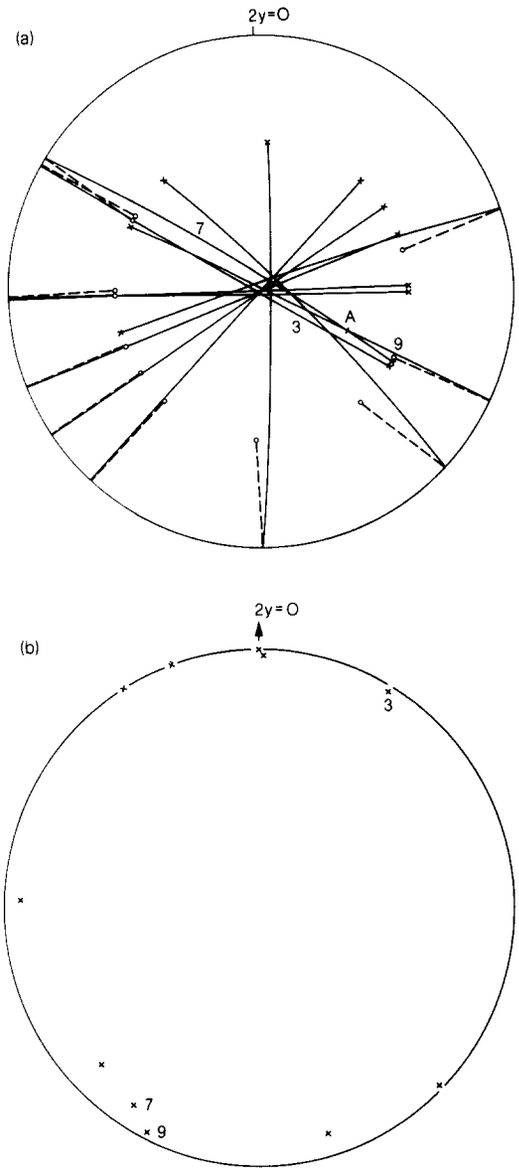

Fig. 10. (a) The $(F, 2y)$ diagram for the data in Table 3, using the half great circle procedure. The labelled point A and the numbered faults are referred to in the text discussion. (b) The equivalent diagram using the pole procedure, as in Fig. 1(c) except that it is the upper hemisphere which is represented for these faults which all have a normal dip-slip component.

1986). We should be particularly wary of interpreting an evolution in palaeostress state in a direction along such a bundle from one knot to another.

(2) The spread of intersections away from the centre of a knot does not in itself cast doubt on the existence or the precision of definition of the knot. Taking Fig. 10(a) as an example, two faults (7 and 9) have an intersection at point A, 40° from the knot's centre. Such deviations are inevitable from curves which lie at an angle of only a few degrees. For each of these faults, we can assume that its generating stress condition lay close to the much higher density of intersections where its curve traverses the knot. The intersection at A is of no consequence.

From these observations, it should be clear that correlation of more than one knot with genuine stress conditions at different stages within the paleostress history requires extreme caution. Even if two genuine knots

exist, there may have been a spatial rather than a temporal separation of the two regimes.

Acknowledgements—All the data used to test the ideas presented here, including the example (Table 3 and Fig. 10) have been generously provided, together with much helpful discussion, by Richard J. Lisle. This paper is improved by the many helpful comments in conscientious reviews by J. L. Simón-Gómez, who spotted a major mistake in one of the examples, and an anonymous referee, who brought the previous use of the angular function of stress ratio to the author's attention. Their assistance is gratefully acknowledged.

REFERENCES

Angelier, J. 1975. Sur l'analyse de mesures recueillies dans des sites faillés: l'utilité d'une confrontation entre les méthodes dynamiques et cinématiques. *C. r. Acad. Sci., Paris* **281**, 1805–1808.

Angelier, J. 1984. Tectonic analysis of fault slip data sets. *J. geophys. Res.* **89**, 5953–5848.

Angelier, J. 1989. From orientation data to magnitudes in palaeostress determinations using fault slip data. *J. Struct. Geol.* **11**, 37–50.

Angelier, J. & Manoussis, S. 1980. Classification automatique et distinction des phases superposées en tectonique de failles. *C. r. Acad. Sci., Paris* **290**, 651–654.

Angelier, J. & Mechler, P. 1977. Sur une méthode graphique de recherche des contraintes également utilisable en tectonique et en séismologie: la méthode des dièdres droits. *Bull. Soc. geol. Fr., Sér.* 7 **19**, 1309–1318.

Armijo, R. & Cisternas, A. 1978. Un problème inverse en microtectonique cassante. *C. r. Acad. Sci., Paris* **287**, 595–598.

Armijo, R., Carey, E. & Cisternas, A. 1982. The inverse problem in microtectonics and the separation of tectonic phases. *Tectonophysics* **82**, 145–160.

Bott, M. H. P. 1959. The mechanics of oblique slip faulting. *Geol. Mag.* **96**, 109–117.

Célérier, B. 1988. How much does slip on a reactivated fault plane constrain the stress tensor? *Tectonics* **7**, 1257–1278.

Carey, E. 1976. Analyse numérique d'un modèle mécanique èlèmentaire appliqué à l'étude d'une population des failles: calcul d'un tanseur moyen de contraintes à partir des stries de glissement. Unpublished thesis, Université de Paris Sud.

Carey, E. & Brunier, B. 1974. Analyse théorique et numérique d'un modèle mécanique élémentaire appliqué à l'étude d'une population de failles. *C. r. Acad. Sci., Paris* **179**, 891–894.

Carey-Gailhardis, E. & Mercier, J. L. 1987. A numerical method for determining the state of stress using focal mechanisms of earthquake populations: application to Tibetan teleseisms and microseismicity of Southern Peru. *Earth Planet. Sci. Lett.* **82**, 165–179.

Etchecopar, A., Vasseur, G. & Daignères, M. 1981. An inverse problem in microtectonics for the determination of stress tensors from fault striation analysis. *J. Struct. Geol.* **3**, 51–65.

Harland, W. B. & Bayly, M. B. 1958. Tectonic regimes. *Geol. Mag.* **95**, 89–104.

Jaeger, J. C. 1969. *Elasticity, Fracture and Flow with Engineering and Geological Applications*. Chapman & Hall, London.

Lisle, R. J. 1987. Principal stress orientations from faults: an additional constraint. *Annales Tectonicae* **1**, 155–158.

Lisle, R. J. 1988. Romsa: a Basic program for paleostress analysis using fault-striation data. *Comput. & Geosci.* **14**, 255–259.

Maxwell, A. S. 1990. Inversion tectonics in the Iberian ranges of Castille-la Mancha, Spain. Unpublished Ph.D. thesis, University of London.

Mercier, J. L. & Carey-Gailhardis, E. 1989. Regional state of stress and characteristic fault kinematics instabilities shown by aftershock sequences: the aftershock sequences of the 1978 Thessaloniki (Greece) and 1980 Campania-Lucania (Italia) earthquakes as examples. *Earth Planet. Sci. Lett.* **92**, 247–264.

Simón-Gómez, J. L. 1986. Analysis of a gradual change in stress regime (example from the eastern Iberian Chain, Spain). *Tectonophysics* **124**, 37–53.

Vergely, P., Sassi, W. & Carey-Gailhardis, E. 1987. Analyse graphique des failles à l'aide des focalisations de stries. *Bull. Soc. géol. Fr., Sér.* 8 **3**, 395–402.

Will, T. M. & Powell, R. 1991. A robust approach to the calculation of paleostress fields from fault plane data. *J. Struct. Geol.* **13**, 813–821.